NANO LETTERS
Cite This: Nano Lett. XXXX, XXX, XXX−XXX
Letter
pubs.acs.org/NanoLett

Kinked Silicon Nanowires: Superstructures by Metal-Assisted Chemical Etching

Georgiana Sandu,[†,¶] Jonathan Avila Osses,[†,¶] Marine Luciano,[‡,¶] Darwin Caina,[†,§] Antoine Stopin,[∥] Davide Bonifazi,[∥] Jean-François Gohy,[⊥] Alejandro Silhanek,[#] Ileana Florea,[▽] Mounib Bahri,[○] Ovidiu Ersen,[○] Philippe Leclère,[◆] Sylvain Gabriele,[‡] Alexandru Vlad,[⊥] and Sorin Melinte*[,†]

[†]Institute of Information and Communication Technologies, Electronics and Applied Mathematics, Université catholique de Louvain, 1348 Louvain-la-Neuve, Belgium

[‡]Interface and Complex Fluids Laboratory, Université de Mons, 7000 Mons, Belgium

[§]Facultad de Ingeniería, Ciencias Físicas y Matemática, Universidad Central del Ecuador, 170521 Quito, Ecuador

[∥]School of Chemistry, Cardiff University, Main Building, Park Place, Cardiff CF10 3AT, United Kingdom

[⊥]Institute of Condensed Matter and Nanosciences, Université catholique de Louvain, 1348 Louvain-la-Neuve, Belgium

[#]Experimental Physics of Nanostructured Materials, Q-MAT, CESAM, Université de Liège, B-4000 Sart Tilman, Belgium

[▽]Laboratoire de Physique des Interfaces et des Couches Minces, Ecole Polytechnique, 91128 Palaiseau, France

[○]Institut de Physique et Chimie des Matériaux de Strasbourg, UMR 7504 CNRS - Université de Strasbourg, 67087 Strasbourg, France

[◆]Laboratory for Chemistry of Novel Materials, Center for Innovation and Research in Materials and Polymers, Université de Mons, 7000 Mons, Belgium

Supporting Information

ABSTRACT: We report on metal-assisted chemical etching of Si for the synthesis of mechanically stable, hybrid crystallographic orientation Si superstructures with high aspect ratio, above 200. This method sustains high etching rates and facilitates reproducible results. The protocol enables the control of the number, angle, and location of the kinks via successive etch-quench sequences. We analyzed relevant Au mask catalyst features to systematically assess their impact on a wide spectrum of etched morphologies that can be easily attained and customized by fine-tuning of the critical etching parameters. For instance, the designed kinked Si nanowires can be incorporated in biological cells without affecting their viability. An accessible numerical model is provided to explain the etch profiles and the physicochemical events at the Si/Au−electrolyte interface and offers guidelines for the development of finite-element modeling of metal-assisted Si chemical etching.

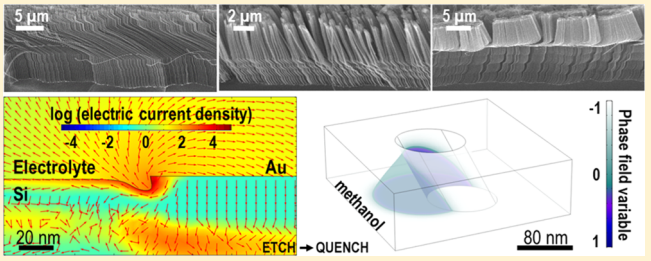

KEYWORDS: *Finite-element modeling, metal-assisted chemical etching, silicon nanowires*

Nanostructures unfold exciting avenues for the well-established Si-based semiconductor industry. Exceptional properties for novel Si-enabled nanomaterials can harness high-performance devices in the fields of electronics, photonics, energy conversion, and storage as well as biotechnology.[1−11] However, the synergy between these properties and their target application requires precise tuning of the characteristic parameters of the nanostructures such as morphology, size, or crystallographic orientation. In particular, controlled design of Si nanostructures, including silicon nanowires (SiNWs), is a prerequisite in order to explore their potential for biomedical purposes. Understanding SiNW−cell interaction has been identified as a subject of primary importance, and seminal work addressed the challenging mismatch between the physicochemical properties of the SiNWs, like topographic features and surface functionalization, and the biological matter. These studies offered insight into the design of substrate-free single SiNWs for integration with biotic and semibiotic systems[12,13] and cellular responses to SiNWs arranged in arrays and three-dimensional architectures.[14−17]

A plethora of techniques were proposed for the reliable fabrication of Si nanostructures and SiNWs.[18−24] Yet, most of these methods require specialized equipment and involve highly sensitive procedures for mass production. In contrast, metal-assisted chemical etching (MACE) associated with a nanostructured continuous catalyst profits from the simplicity of the electroless etching process while allowing for the control of

Received: June 25, 2019
Revised: September 15, 2019
Published: October 8, 2019

DOI: 10.1021/acs.nanolett.9b02568
Nano Lett. XXXX, XXX, XXX−XXX

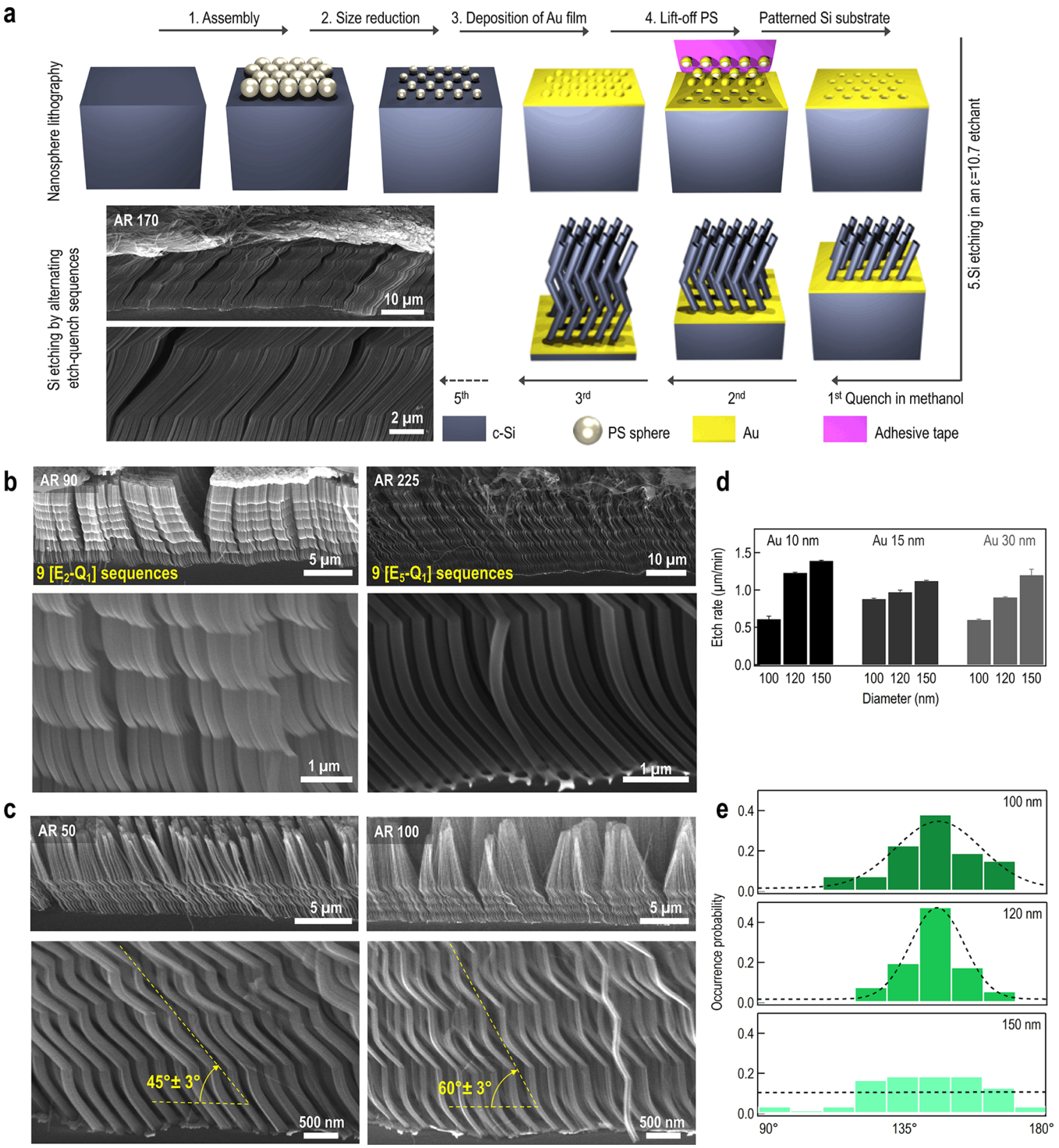

Figure 1. MACE details. (a) Sketch of MACE for synthesis of k-SiNWs. First, the Si substrate is patterned with a holey Au mask by PS nanosphere lithography. Second, the nanostructuring of Si follows repetitive etch-quench $[E - Q]$ sequences. The SEM pictures show the k-SiNWs with s = 120 nm resulted after five successive $E_5 - Q_1$ sequences. (b) High aspect ratio k-SiNWs fabricated by $9[E_2 - Q_1]$ (left) and $9[E_5 - Q_1]$ (right) sequences for a t = 15 nm, s = 120 nm Au mask. (c) The longitudinal axis of the k-SiNWs deviates by different angles with respect to the Si substrate, depending on the diameter of the Au mask openings [150 (left) or 100 nm (right)]. The Au mask is 10 nm thick. (d) Etching rates associated with the geometrical parameters of the Au masks. (e) Occurrence probability for the observed kink angles as a function of s. The dashed lines in the histograms are fits of experimental data and are only intended as guides to the eye.

various parameters: morphology (solid or porous), diameter, length, and to a certain extent, crystallographic orientation.[18,21,25−29] MACE essentially works as a localized, short-circuited, galvanic cell comprising an intimately connected Si anode with a nanoshaped catalyst cathode in a hydrofluoric acid (HF) and hydrogen peroxide (H_2O_2)-based electrolyte that controls both the H_2O_2 reduction and Si dissolution.

Although the general understanding of MACE emphasizes on the anisotropic ⟨100⟩-etching predisposition as prescribed by the backbone theory, non-⟨100⟩ SiNWs have been demon-

DOI: 10.1021/acs.nanolett.9b02568
Nano Lett. XXXX, XXX, XXX−XXX

strated, regardless of the initial Si wafer orientation.[25] In particular, hybrid orientation SiNWs or kinked SiNWs (k-SiNWs) are extremely interesting from both theoretical and experimental standpoints considering their morphology that has a positive impact on the photon absorption, elastic properties, as well as thermal insulation.[27,30−32] Targeted hybrid peptide−k-SiNWs can be tailor-made from optimized directed assembly of biological matter[12,33] with kinks, diameter modulations, and asymmetric features adapted to the viscoelastic response of the cellular membranes. In this context, the development of simple approaches that allow for large-area, controlled fabrication of k-SiNWs is essential for exploring their physical properties and enable their use as building blocks in complex patterned environments.[34−36] Along this direction, several reports analyzed advanced etching schemes to control the etching direction and ultimately engineer custom crystallographic superstructures.[37−40] Temperature and oxidant agent concentration were identified as critical parameters for suppressing the preferred ⟨100⟩ etching direction. For instance, temperature control of the electrolyte was used to wafer-scale, zigzag etch of the SiNWs on (111)-Si wafers.[40] Alternating between different etching solutions with different oxidant concentration allows the etching of orientation-modulated SiNWs on (111)-Si wafers.[25] The etching would follow ⟨100⟩ etching at low oxidizing agent concentration and non-⟨100⟩ etching at higher concentrations.

Similarly, a recent report also details the controlled fabrication of k-SiNWs via the use of various electrolytes where the etchants' availability is constrained because of additives in the etching environment.[37] Addition of high surface tension additives like glycerol can greatly alter the availability of etchants creating diffusion barriers for the chemical species. Indeed, the miscibility of the etchants is a critical MACE parameter in particular for etching conditions without mechanical agitation. As a matter of fact, the kinks are almost exclusively associated with static etching conditions, whereas stirring typically renders vertical ⟨100⟩ SiNWs because the etchants are continuously replenished. However, such a procedure cannot account for reliable large-scale fabrication of high aspect ratio k-SiNWs, ubiquitously required for surface-to-volume sensitive applications, considering that the induced perturbations are local and difficult to control. Because Si MACE is a dynamic process with parameters changing as the etching advances, controlling the etching patterns to produce k-SiNWs, such as deviating the catalyst motion and turning on and off crystallographic dependencies are particularly challenging. For instance, the noble metal catalyst plays a fundamental role in MACE, accelerating the dissolution of Si in the areas where an intimate contact is preserved while exclusively dictating the features of the resulting nanostructures such as shape and crystallographic orientation. Although the motion of catalyst is uniform, it can be ruled by its shape: a metal nanoparticle has six degrees of freedom, whereas a pinned catalyst such as a rigid, contiguous mask is able to move with three degrees of freedom, two translational components and one rotational. Template-based MACE with nanopatterned Au masks is the landmark for large-scale, controlled fabrication of SiNWs and k-SiNWs. Thus, assessing the impact of the catalyst shape on the etched morphologies is critical for developing a reliable synthesis of Si superstructures.

Here we describe a simple and efficient k-SiNWs etching scheme that facilitates the fabrication of high aspect ratio Si superstructures with hybrid crystallographic orientation. This etching mechanism relies on repetitive etch-quench sequences to induce the kinks using low surface tension ethanol cosolvent. Multiple etching baths are no longer required as the etchant availability is modulated via the methanol quencher, and risks related to the etchant baths' imbalance at advanced etching stages are reduced. This one-pot-type synthesis facilitates the etching of mechanically stable, high aspect ratio superstructures at high etching rates. The systematic assessment of the main MACE parameters, namely Au mask thickness coupled with the opening diameter, has allowed the etching of a wide spectrum of nanostructures. We highlight that the development of well-controlled morphology k-SiNWs could help uncover cellular responses and interactions with extracellular matrix. Experimental data are coupled with a numerical model to explain the etched morphologies as well as the observed kink angles. We particularly emphasize (i) mass transport of the chemical species, (ii) Si interfaces from an electrical charge transport perspective, (iii) flow and passive mixing in microchannels delimited by k-SiNWs, and (iv) the general mechanism for the k-SiNWs formation. The knowledge provided here helps to clarify the mechanism of the kinks' formation and enables large-scale fabrication of high aspect ratio k-SiNWs, while establishing novel guidelines for the development of MACE complex numerical simulations.

Controlled k-SiNWs Synthesis. Figure 1a presents a route for the controlled fabrication of k-SiNWs with high aspect ratio (AR), enabled by a simple MACE scheme. The first step is the nanopatterning of the Au catalyst mask via colloidal lithography. This operation requires the self-assembly of closed-packed polystyrene (PS) spheres of 260 nm in diameter on the Si substrate. The PS spheres are further etched with reactive ion etching to the desired size representing the final diameter of the SiNWs. Subsequently, the Au catalyst is deposited on the PS-decorated Si substrate. The nanopatterned Au mask is obtained by lift-off of the PS spheres with adhesive tape. The next step is the Si etching in a solution having a molar concentration ratio $\varepsilon = 10.7$ of HF to H_2O_2, with ethanol as cosolvent, under static etching conditions. To form the kinks at the desired location, Si etching is interrupted at specific times by submersing the sample in methanol. Varying these etch-quench sequences at specific times renders superstructures of k-SiNWs; E_p is used for designating an etching step with the etching time of p minutes and Q_q for a quenching event lasting q minutes. The number of kinks n is simply controlled by the performed $(n + 1)[E - Q]$ sequences. The cross-section scanning electron microscopy (SEM) pictures in Figure 1a show highly ordered k-SiNWs fabricated by five sequences $E_5 - Q_1$. On the one hand, by altering the etching time we can control the length of the etched segment and, related to this, the location of the kink. On the other hand, the geometrical parameters of the gold catalyst mask are extremely important. They will influence the porous or solid nature of the etched Si nanostructures, the etching rate as well as the mechanical stability of the Au mask during the downward movement and the gas evolution reactions associated with Si etching. As a matter of fact, catalysts greatly impact the mass transport of active species and reaction products.[18] For instance, as the catalyst thickness decreases, transport of reactants and byproducts is expected to occur also via small pores in the catalyst. In addition, collision and coalescence of gas bubbles can alter the Si-catalyst contact resulting in hazardous etching and, ultimately, in catalyst delamination. To get insight into the etching possibilities provided by various catalyst morphologies, we evaluated different catalyst thicknesses, t (10, 15, and 30 nm), associated with different opening

DOI: 10.1021/acs.nanolett.9b02568
Nano Lett. XXXX, XXX, XXX−XXX

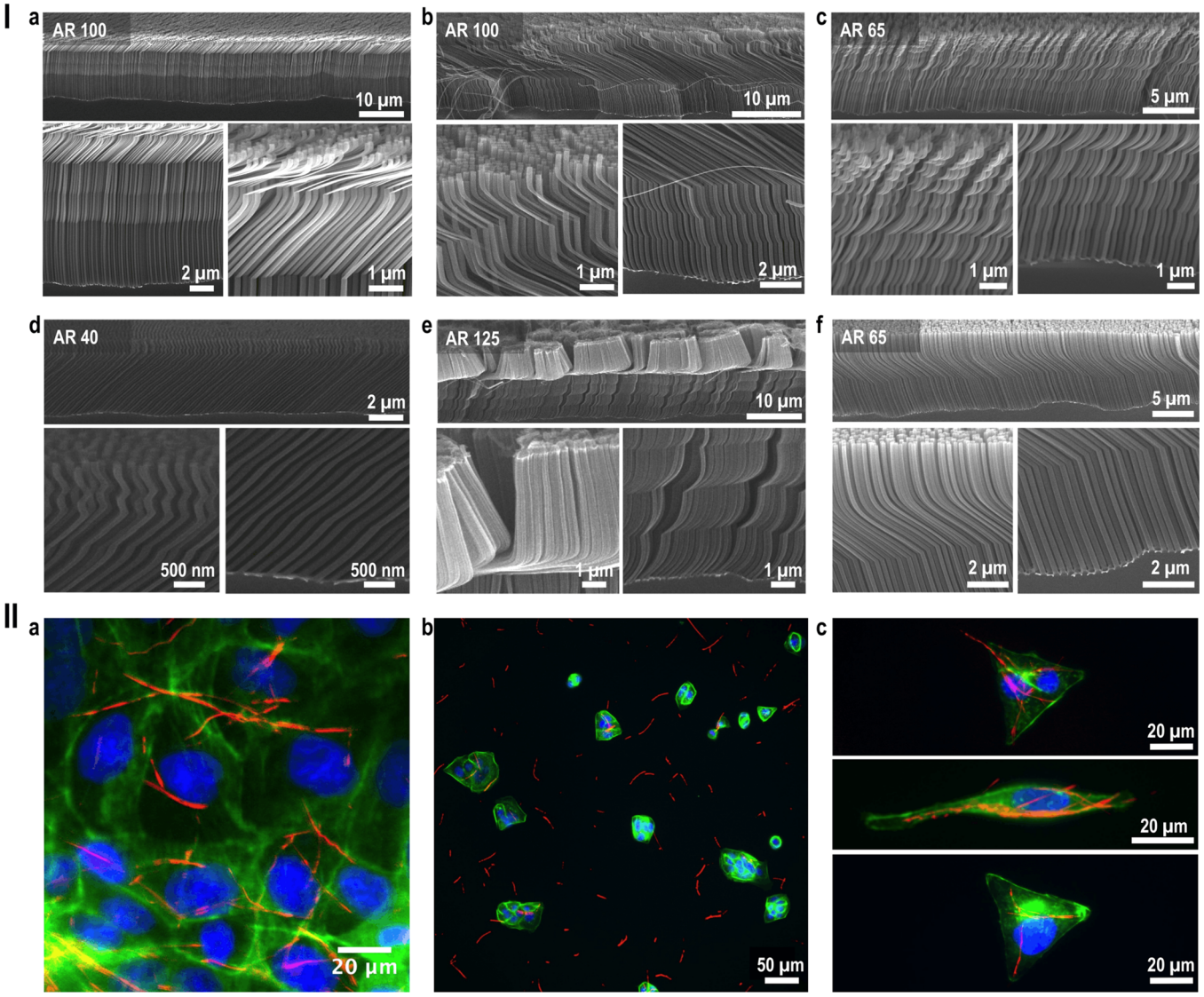

Figure 2. (I) A wide spectrum of morphologies can be achieved by superposing different etching times with different catalyst shapes. (a) t = 30 nm, s = 150 nm, $E_p - Q_1$; p = {5,3,3,3,5}. (b) t = 15 nm, s = 120 nm, $E_p - Q_1$;p = {5,7,3,3,3}. (c) t = 30 nm, s = 120 nm, $E_p - Q_1$; p = {2,2,2,3,3,3}. (d) t = 30 nm, s = 120 nm, $E_p - Q_1$; p = {3,2,2,2,2}. (e) t = 15 nm, s = 120 nm, $E_p - Q_1$; p = {5,3,3,3,3}. (f) t = 30 nm, s = 150 nm, $E_p - Q_1$; p = {5,5}. (II) Interfacing k-SiNWs with mammalian cells. (a) k-SiNWs (red) distribution and their intra- and intercellular interfaces in a dense culture media. (b) Penetration of k-SiNWs into individual cells seeded on micropatterned substrates. (c) k-SiNWs interfacing with nucleus (blue) as well as the actine cytoskeleton (green).

diameters, s (100, 120, and 150 nm). Details of the deposited Au mask morphologies are shown in Figure S1.

Kink Physical Parameters. Figure S2 shows the kink formation according to the number of times the reaction was quenched for a 10 nm thick Au mask and three different hole diameters. For this particular case, vertically aligned NWs are obtained for the first E_2 segment. The type of the first segment is particularly intriguing: vertical NWs are obtained only for thin Au masks, whereas for larger Au thickness the etching proceeds in a non-⟨100⟩ direction, as illustrated in Figure S3. After a 2 min quenching time, the etching proceeds in a non-⟨100⟩ direction, leading to a kink formation. To characterize the kink, its segments' length and angle have to be considered in relation to the Au mask's geometrical parameters. For this study, to control the kink's segment length, we used etching times, p, ranging from 2 to 5 min. The k-SiNWs fabricated by nine repetitive $E_2 - Q_1$ and $E_5 - Q_1$ sequences are shown in Figure 1b for a t = 15 nm and s = 120 nm Au mask. Figure 1c shows the k-SiNWs fabricated with a 10 nm thick Au mask with s equal to 150 and 100 nm and reveals the tilted nature of the k-SiNWs, dictated by s. Note that the length is reported as the etching depth of the Si substrate, normal to the surface. The average etching rates evaluated for various t and s are shown in Figure 1d. The highest etching rates are obtained for thin catalysts because the active species can easily diffuse along the grain boundaries. The etching rates are found to generally increase as s increases. Specifically, the highest etching rate reaches 1.4 μm per minute for t = 10 nm, s = 150 nm Au masks because less Si has to be removed. Such fast etching rates are not common for MACE because aggressive gas evolution leads to Au mask delamination. The quenching step mitigates hazardous etching and maintains etching speed accuracy as discussed later.

The angles of the kinks are found to be dependent on s, as it can be observed from the statistical analysis of Figure 1e. Thus,

DOI: 10.1021/acs.nanolett.9b02568
Nano Lett. XXXX, XXX, XXX−XXX

for small diameters there is a clear angle preference, whereas for bigger diameters a wide range of angles is possible. The dependency of the kink angle as a function of metal mask thickness was further evaluated: t does not appear to influence the distribution of the kink angles, as shown in Figure S4.

Finally, note that kinks will also form by employing a thin catalyst mask with a random pattern (Figure S5). Thus, kink generation does not require a uniformly patterned or a pinned catalyst. Nonetheless, the stability of the mask is expected to be affected by gas bubble evolution leading to the loss of Si−Au contact and eventually to Au exfoliation and the end of the etching (Figures S4 and S5).

Customized Si Superstructures. Our etching protocol combines the simplicity and scalability of MACE to enable functionality-driven design of Si nanostructures. Figure 2 shows the fabrication of ordered, high aspect ratio superstructures of k-SiNWs by quenching the etching at user-defined points during MACE. These results indicate that k-SiNWs and complex Si nanostructures with a large range of angles and user-defined segment lengths are possible by simply controlling the etching time and the catalyst parameters. The catalyst mask parameters are intimately coupled with the etching rates and curvature effects and will greatly influence the k-SiNWs morphology. SEM images in Figures S6 and S7 provide further information on the etching opportunities of this procedure. Zigzag SiNWs are locally observed under the studied etching conditions as shown in Figure S8. Once a SiNW segment is etched, the electrolyte concentration is altered by flushing the sample with methanol. Flushing with water renders highly porous SiNWs as displayed and further discussed in Figure S9 and Figure S10. Such versatile fabrication opens extensive research possibilities to fully explore and activate the properties of these Si superstructures.

We highlight key fabrication features of MACE strategies developed for k-SiNWs and high aspect ratio Si superstructures in Table 1. Although k-SiNWs can be formed by several MACE methods, the geometrical parameters remain hard to control with kinking or NW diameter and segment modulation being randomly (or progressively[37]) attained. The present one-pot synthesis technique offers precise control over the segment length and aspect ratio, reaching values commonly observed in studies with mechanically clamped catalysts.[41] Note that the morphology of the surface plays an important role in establishing the overall mechanical properties of SiNWs. In this respect, the possibility to generate, besides diameter modulations during synthesis,[42,43] a catalyst-dense coating as functional layer is peculiarly appealing.

Table 1. Overview of MACE Protocols Enabling k-SiNWs and High Aspect Ratio Si Structures

details	type	AR	surface	source
vertical directionality-controlled[a]	SiNWs	>100:1	smooth	ref 41
nanoshaped catalyst-driven[b]	k-SiNWs	>∼20:1	smooth (rough)	refs 25,38−40,44
diffusion-controlled[c]	k-SiNWs	>∼20:1	smooth	ref 37
one-pot synthesis	k-SiNWs	>200:1	smooth (rough)	this work

[a]The catalysts are mechanically clamped during the process. [b]Patterned metal catalysts display superior performances compared to nanoparticle based catalysts. [c]Zigzag SiNWs can be formed as well above a critical nanowire length of about 1 μm.

High aspect ratio SiNWs and k-SiNWs as well as Si superstructures obtained by MACE enabling straightforward cell internalization experiments are essentially missing, as specific applications demand different categories of k-SiNWs.[45] The combination of biological cells and SiNWs has been recognized as an efficient way to control the differentiation of stem cells by modulating the activation of Ca^{2+} ion channels in response to a mechanical stimulation at the nanoscale,[46] and scaffolds of SiNWs could provide unique shape- and composition-controlled sensing interfaces for cells.[47] To address these issues, we carried out a series of experiments with epithelial cells (Supporting Information). In agreement with previous work on embryonic stem cells and human embryonic kidney cells,[14] our results indicate that the penetration of the as-fabricated k-SiNWs into individual epithelial cells naturally occurred during the incubation without affecting their viability. The 120 nm diameter k-SiNWs started to internalize within 45 ± 15 min in epithelial cells and the number of incorporated nanowires doubled after 120 min of incubation. The surface functionalization of the nanowires with peptides or proteins that can bind to transmembrane integrins is certainly an interesting way to quicken k-SiNW cell internalization.[17] Such Si superstructures can be further sharpened into a compelling tool for studying intra- and intercellular biological processes and deciphering complex mechano-transduction pathways.[48]

Vizualization of Si superstructures was accomplished by transmission electron microscopy (TEM). Figure 3a shows results obtained for a 15 nm Au mask for all studied s values. It is clear that the initial SiNW diameters are altered by the horizontal movement of the catalyst. The deviations from the initial diameter are more important as s increases. Furthermore, the Au catalyst oscillatory motion is clearly visible in the SiNW wall close up from Figure 3b and also revealed by the 3D reconstruction of the SiNW kink (Figure 3c). The expected cylindrical shape is altered, confirming the horizontal shift of mask in addition to the downward movement associated with the Si etching. This behavior mirrors the three-directional motion expected for a weakly pinned catalyst. In addition, a closer examination of the SiNWs, Figure 3b,d, shows that their surface is decorated with Au nanoparticles, some of them reaching ∼15 nm in diameter for thick Au catalysts, as displayed in the inset to Figure 3d. This relates to energetic etching conditions that can attain rates as high as ∼20 nm/s, inducing significant mechanical stress into the metal layer, finally leading to Au disintegration. Note that the Au nanoparticles couple to the surface of SiNWs (Figure S11). The elemental mapping from Figure 3e confirms the Au decoration of k-SiNWs. This feature, as highlighted in Figure 2, is particularly interesting for biological applications where Au-decorated SiNWs are known for their distinctive photothermal response under near-infrared laser irradiation, which can potentially be used for the destruction of cancerous cells.[49] Porous trenches form in the Si substrate, beneath the Au, at the lithographic openings of the metal catalyst (Figure 3e, Figure S12). Such porous regions are known to facilitate diffusion of the electrolyte.[50] In addition, the shape of the porous trenches hints at an anisotropic kinetics or a preferential electrolyte diffusion via the lithographic openings of the Au mask. This is surprising because mass transport of reactants usually occurs via pores or cracks in thin films or discontinuous catalyst masks, therefore an isotropically expanded porous segment at the metal−Si interface is expected.[51] In particular, the porous region does not extend completely to the foot of the SiNW as previously reported.[50]

DOI: 10.1021/acs.nanolett.9b02568
Nano Lett. XXXX, XXX, XXX−XXX

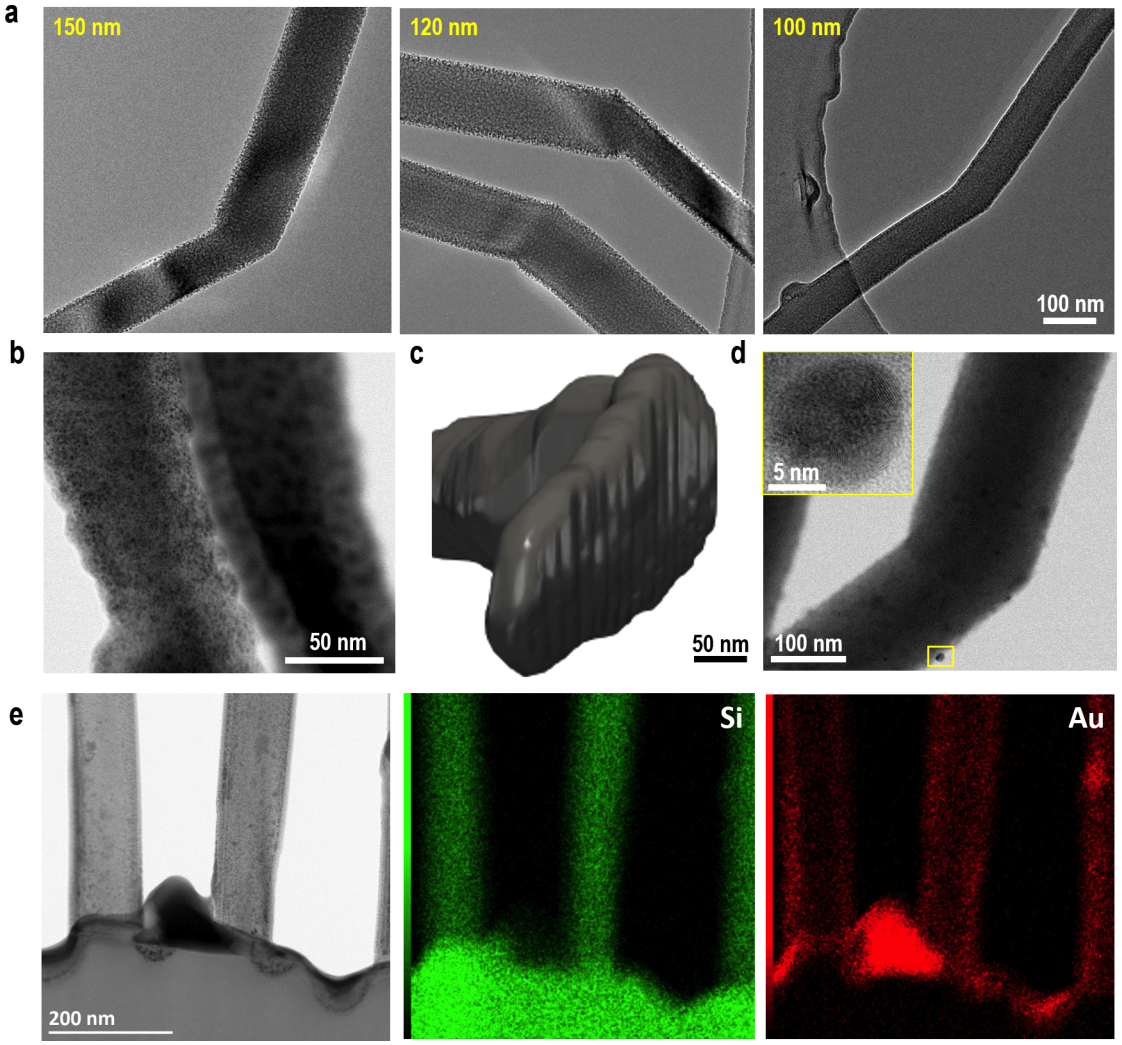

Figure 3. Microscopic characterization of SiNW kinks and Si−Au interface. (a) TEM images of SiNW kinks obtained from the indicated *s* with *t* = 15 nm Au masks. (b) SiNW kink close up as imaged with scanning TEM (STEM) with a bright field detector for the *s* = 100 nm, *t* = 10 nm Au mask. (c) Three-dimensional reconstruction of a SiNW kink obtained with the *s* = 150 nm, *t* = 30 nm Au mask. (d) Au nanoparticles-decorated SiNW kink produced by the *s* = 100 nm, *t* = 30 nm Au mask. (e) Elemental mapping by energy-dispersive X-ray spectroscopy of the Au−Si interface via STEM.

Analysis and Modeling. The broad spectrum of the etched Si superstructures suggests a synergy between various physicochemical processes depending on the characteristic dimensions of the Au−Si system. Metal-assisted chemical etching resides on a noble metal catalyst to accelerate the dissolution of Si into a HF and H_2O_2-based electrolyte by generating instantaneous electrical currents flowing between cathodic sites where H_2O_2 is reduced and the anodic sites where Si is oxidized and further dissolved. Under the current understanding, the etching proceeds with the catalytic decomposition of H_2O_2 providing the holes (h^+) that are further required for Si oxidation, facilitating its dissolution. The etching is an uninterrupted process as the catalyst protected Si is continuously etched leaving the SiNWs as residues on the Si substrate. Thus, MACE is associated with the movement of the catalyst that needs to preserve an intimate contact with the Si substrate.

Etching Parameters. We performed time-dependent numerical simulations following the current understanding of MACE. The two-dimensional (2D) system used for the finite-element model is shown in Figure 4a,d and represents a projection of a Si substrate partially covered with a Au mask in contact with the HF and H_2O_2-based electrolyte. The Si−Au interface is described by the Schottky junction model.[51,52] The electrolyte is modeled here as an ohmic solution with the kinetics of the electrolyte interfaces, that is, with Si and Au, governed by Butler−Volmer expressions.[53]

It is well-known that chemical etching of silicon in HF solutions proceeds very slowly without an external potential.[52] If holes are readily available, Si dissolution can proceed according to

$$Si + 4HF_2^- + 2h^+ \rightarrow SiF_6^{2-} + 2HF + H_2 \quad (1)$$

This reaction has a potential of −1.24 V (versus standard hydrogen electrode). The availability of holes will be determined by the electrical polarization and properties of the silicon. For this case, the electric polarization is provided by the positive charge generated via the Au mask by the reduction of hydrogen peroxide

$$H_2O_2 + 2H^+ \rightarrow 2H_2O + 2h^+ \quad (2)$$

This reaction has a potential of +1.76 V (versus standard hydrogen electrode). Because of the Schottky barrier, not all the positive charges can be drained into the silicon, therefore, a

DOI: 10.1021/acs.nanolett.9b02568
Nano Lett. XXXX, XXX, XXX−XXX

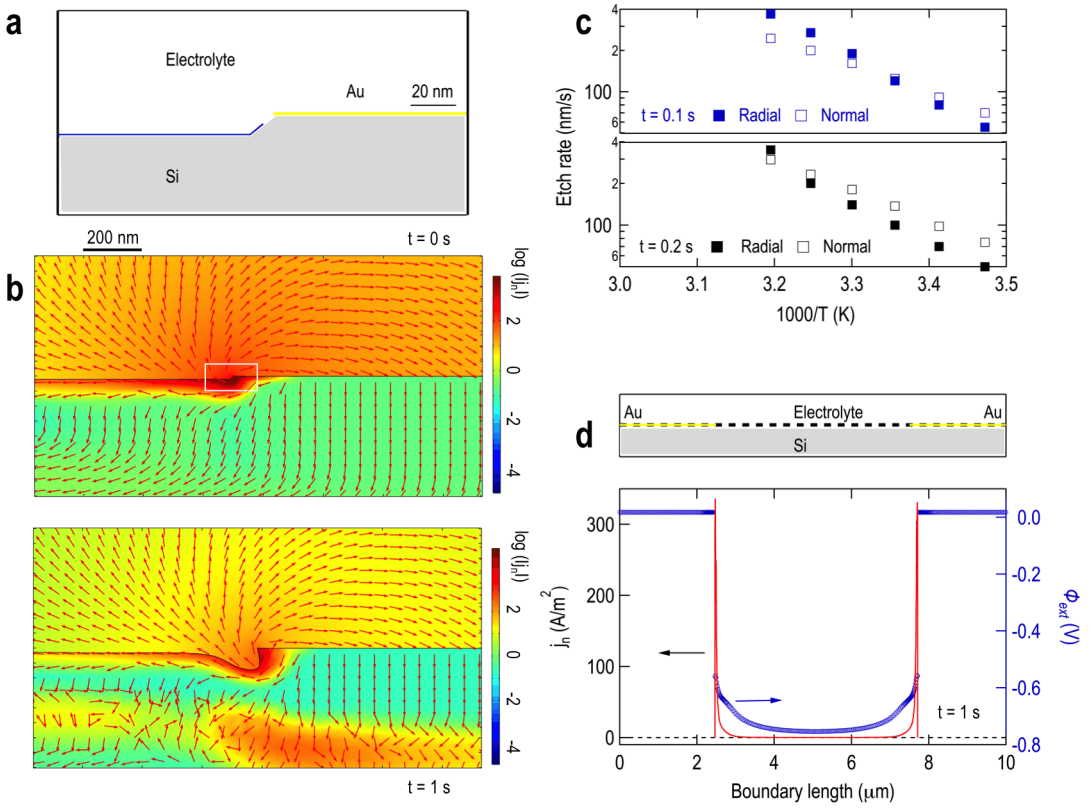

Figure 4. Time-dependent numerical calculations of Si MACE. (a) Zoom into the bidimensional domain used for the finite-element model. It includes a pre-etched line in the Si-electrolyte boundary. The blue line corresponds to the conducting Si−electrolyte boundary, whereas the yellow line to corresponds to the Si/Au−electrolyte boundary. To avoid exceedingly high electric field values, these boundaries are separated by a 10 nm gap. (b) Electric current density profiles (logarithmic scale) at t = 0 and 1 s etching advancements. The highlighted rectangle corresponds to the area zoomed in panel a. (c) Temperature and time dependence of the etching rates associated with radial and normal etching directions. (d) Two-dimensional sketch representing the interfaces included in the calculation. ϕ_{ext} (blue curve) and electrical current density (red curve) corresponding to t = 1 s.

positive potential is expected on the Au side. Moreover, a positive potential buildup is also favored due to the relationship of the reduction potentials. Butler−Volmer dependences[53] relate the module of the outgoing, normal-to-interface, current density $|j_n|$ to the external potential ϕ_{ext}, the electrolyte potential ϕ_l, and the equilibrium potential at the electrodes ϕ_{eq} (see Supporting Information).

Figures 4b shows the calculated electric current density and etching profiles. The etch rate is around 100 nm/s at room temperature for both the in-plane (radial) and the out-of-plane (normal) directions with small differences due to the electrical current density variation with the distance from Au. Because the electrical current is maximum near the Au border due to the high electric field there, the highest etching rate will be close to Au (Figure 4b). These numerical profiles are in agreement with the experimental observations of Figure 3e, confirming the lithographic openings of the metal catalyst as hot spots for the Si etching. The calculated etching rates display the expected dependence with temperature (Figure 4c). For $j_n \cong 300$ A/m^2 at t = 1 s, a normal etch rate of 1.125 μm/min is observed, closer to the experimentally observed etch rates at large s, 1.25 ± 0.15 μm/min. The reactions at the electrolyte interfaces generate an electric potential difference that is seen in Figure 4d. This electric potential difference is lower than the open circuit potential $\phi_{eqAu} - \phi_{eqSi}$ due to the electrical current circulating in the electrolyte. The electrical current density has maxima near the Au mask border (Figure S11).

The adopted model provides insight into the experimental trends, although it relies on ideal interfaces. Although isotropic properties are assumed in the model, it is clear that the normal-to-interface etching is preferred in the realistic three-dimensional environment. The etching direction is expected to be a vector combination of both normal and radial directions. Local variations of the etching conditions such as the chemical species' availability or local heating will likely influence which component controls the etching direction. Indeed, while the experimental observations indicate that s plays a subtle role in the etching direction preference (Figure 1c), the present numerical calculations unveil the time and temperature dependencies of the radial and normal etch rates. From the numerical calculations we can estimate an electrolyte−Si Schottky barrier of ∼0.45 V (Figure S14). Although the SiNW kinks formation clearly implies a deviated catalyst motion, the employed model ignores the catalyst motion, because the driving force is still unknown.

Kink Formation. We turn next to SiNW kink formation. Figure 5a shows snapshots of the advancements of the wetting front for methanol and water in k-SiNWs relevant superstructures. For k-SiNWs morphologies, methanol completely wets the sample after 16 s, whereas water travels only half of the sample length. Liquid invasion follows a diffusion law with parameters dependent on the structural geometry of the SiNWs[54]

$$z = \sqrt{Dt} \tag{3}$$

DOI: 10.1021/acs.nanolett.9b02568
Nano Lett. XXXX, XXX, XXX−XXX

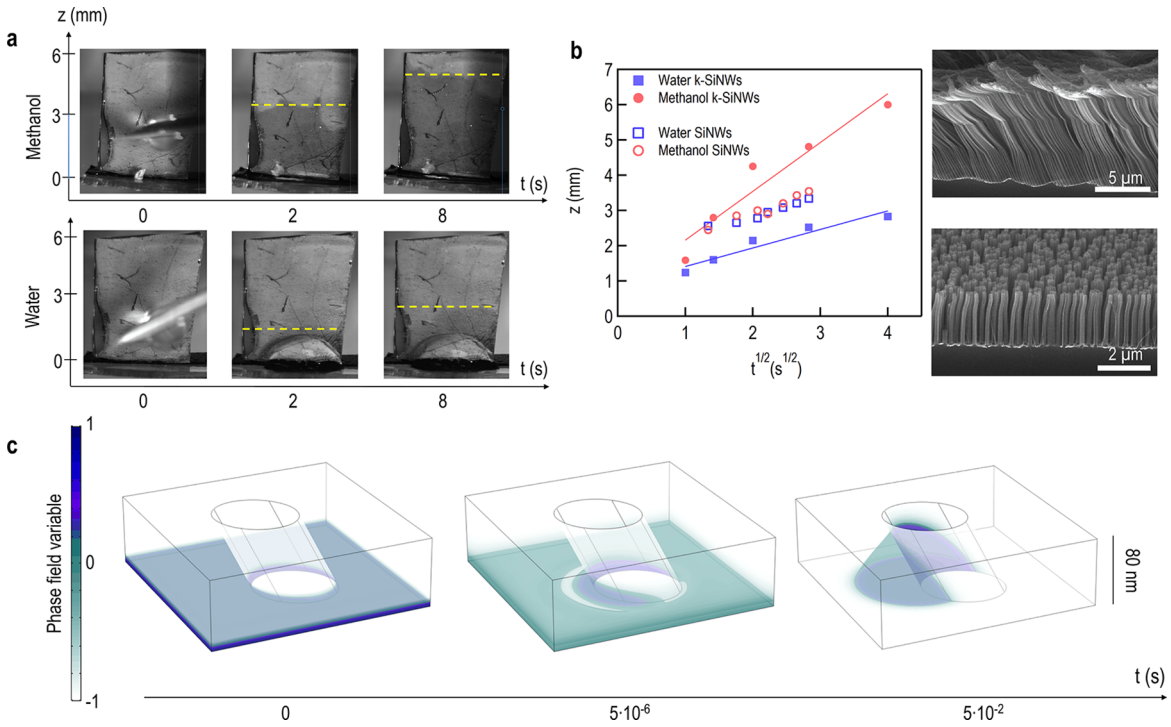

Figure 5. Wetting properties. (a) Macroscale: Snapshots of the distance traveled by the wetting front for water and methanol in Si superstructures. (b) Plot of the distance traveled by the etching front with $t^{1/2}$ for water and methanol wet samples [k-SiNWs (closed symbols) vs SiNWs (open symbols)]. (c) Nanoscale: Time evolution of methanol boundary around a 60° tilted SiNW, with a diameter of 100 nm, as resulted from numerical calculations with periodic boundary conditions. The color bar indicates the phase field variable. The final configuration is persistent.

where z is the displacement of the wetting front, t is the time, and D is a coefficient that captures the characteristic velocity of the liquid and the viscous forces developed according to the wetting geometry. From Figure 5b, we can conclude that 1 min quenching will remove all the electro-active species required for the etching of k-SiNWs. Furthermore, if the SiNW etched segment is tilted, there is a preferential formation of a methanol rich meniscus in the concave part of the nanowire base as shown in Figure 5c. This preferential accumulation of methanol results in the retarded action of the etchants when the etching resumes. The local concentration of species is altered, triggering a change in the etching direction.

For numerical calculations, two phases are considered, namely, methanol and air, in contact with a nanowire of 100 nm diameter and its base. A continuous phase field model based on the Cahn−Hilliard[55,56] equation is used, considering the surface tension $\sigma_{ma} = 22.7$ mN/m^2 of the methanol−air interface and $\theta_c = 60°$ contact angle for the methanol−Si interface (Figure S10). Further details can be found in the Supporting Information. In the initial configuration, the methanol is a uniform layer of 7 nm height surrounding the base of the SiNW. As time runs, the methanol rises on the inner part for a tilted SiNW with respect to the substrate, receding on the other side, as can be seen in Figure 5c. This droplet not only modifies the concentration of the etchants, it also can exert a pull up force on the underlying Au film, changing the etching conditions and contributing to the etch direction change. Note that meniscus formation along vertical SiNW segments does not show any preferential location (Figure S15). Because the the contact angle for the liquid−Si interface is expected to evolve as the etching advances, we evaluated the meniscus formation at different contact angles to account for any changes in this parameter (Figure S16, 60°-tilted SiNW). The meniscus formation around a 45°-tilted SiNW for different contact angles is shown in Figure S17. There is a clear preferential location for the meniscus formation, except for low θ_c where the methanol layer rather uniformly surrounds the SiNW. However, a low contact angle scenario is unlikely since the surface roughness of the SiNWs is expected to increase θ_c.

The curvature of the SiNW kink segments is an intriguing phenomenon and the etching of curved SiNWs has been associated with cosolvent etchants such as methanol, ethanol, or glycerol.[37,57,58] While experimental observations sustain the curvature dependence with the cosolvent concentration, curved segments are typically linked to large thicknesses and large diameter openings of the Au mask. MACE begins as a thermodynamically favored process, however, as the etching advances other forces interfere with the reactions. First, methanol meniscus formation will alter the concentration of species at the Si−electrolyte interface. Once the etchant concentration is re-established, the etching resumes. Second, the etched geometry is expected to impact both the electrolyte flow as well as the quenching agent flow as the etching advances, giving rise to parasite capillarity and viscous forces. The curvature formation has to be associated with the development of directional forces related to the NW geometry. As the etched geometry develops into opened zigzag nanochannels, it is well-known that these are prone for developing turbulent flow, providing efficient mixing of electrolyte and quenching agent. This explains the fact that the SiNW kink angles are increasing with the etched length.

In summary, we described the versatility of MACE to fabricate high aspect ratio and orientation-customized k-SiNWs based on successive etch-quench sequences. We found that the parameters of the catalyst Au mask greatly influence the geometry and porosity of the etched Si superstructures. On the

DOI: 10.1021/acs.nanolett.9b02568
Nano Lett. XXXX, XXX, XXX−XXX

one hand, the opening diameter impacts the etching rate and the overall kink angle distribution. On the other hand, the thickness of the Au mask has a pronounced effect on the porosity of the produced nanostructures and small catalyst thicknesses are not suitable for long etching times. Fine tuning of these parameters have allowed the etching of functionally designed, complex Si nanostructures with high aspect ratio. Focusing on the quenching step, we propose a simple mechanism for kink formation through preferential formation of an alcohol-rich meniscus in the concave region of the etched Si segment. Our time-dependent calculations corroborate the current understanding of the mechanisms involved in MACE of Si and represent another step toward more complex finite-element models for Si superstructures corrosion. The numerical computing approach could be extended to other electrochemical systems requiring modeling of the semiconductor electrode−electrolyte interfaces. Although we used the fabricated k-SiNWs in a substrate-free approach to address cell internalization, the Si superstructures can be employed, for example, in frustrated phagocytosis experiments to shuttle biomolecular cargo once the density and diameter are matched to the cell size and the aspect ratio is tuned for cellular adhesion and penetration. Our findings open extensive opportunities for Si superstructures tailored for enhanced functionalities and encourage numerical investigations for understanding the MACE fundamentals.

■ ASSOCIATED CONTENT

Supporting Information

The Supporting Information is available free of charge on the ACS Publications website at DOI: 10.1021/acs.nanolett.9b02568.

Insight into the experimental procedures and details of the numerical calculations (PDF)

Representative movie of the electric current density evolution at the Si−Au interface during initial stages of metal-assisted chemical etching. Frame rate is 16 images/s and total length is 6 s (AVI)

■ AUTHOR INFORMATION

Corresponding Author

*E-mail: sorin.melinte@uclouvain.be.

ORCID

Davide Bonifazi: 0000-0001-5717-0121

Jean-François Gohy: 0000-0003-4169-1883

Ovidiu Ersen: 0000-0002-1553-0915

Alexandru Vlad: 0000-0002-0059-9119

Sorin Melinte: 0000-0003-2176-554X

Author Contributions

¶G.S., J.A.O. and M.L. contributed equally to this work.

Notes

The authors declare no competing financial interest.

■ ACKNOWLEDGMENTS

We are grateful to the Walloon Region for financial support in the frame of the "BATWAL" project - "Programme d'Excellence". Work has been carried out within the project LUMINOPTEX (avec le soutien du Fonds Européen de Développement Régional/met steun van het Europees Fonds voor Regionale Ontwikkeling - INTERREG V France-Wallonie-Vlaanderen). The work was supported by the Belgian F.R.S. - FNRS in the frame of the research conventions no. T.1004.14 and no. T.0106.16. This research connects to the ARC project entitled "BATTAB" (research convention no. 14/19-057) sponsored by the Communauté Française de Belgique. M.L. is financially supported by FRIA. S.G. is supported by the Belgian National Fund for Scientific Research (F.R.S. - FNRS, Crédit de Recherche - J009916F) and FEDER PROSTEM. M.B. and O.E. would like to thank the French ANR (National Research Agency) under the 3DCLEAN project 15-CE09-0009-01 for financial support. S.M. and P.L. are Research Associate and Senior Research Associate of the Belgian F.R.S. - FNRS, respectively.

■ REFERENCES

(1) Rurali, R. *Rev. Mod. Phys.* **2010**, *82*, 427−449.

(2) Glassner, S.; Zeiner, C.; Periwal, P.; Baron, T.; Bertagnolli, E.; Lugstein, A. *Nano Lett.* **2014**, *14*, 6699−6703.

(3) Park, H.; Crozier, K. B. *ACS Photonics* **2015**, *2*, 544−549.

(4) Wang, Y.; Wang, T.; Da, P.; Xu, M.; Wu, H.; Zheng, G. *Adv. Mater.* **2013**, *25*, 5177−5195.

(5) Tsakalakos, L.; Balch, J.; Fronheiser, J.; Korevaar, B. A.; Sulima, O.; Rand, J. *Appl. Phys. Lett.* **2007**, *91*, 233117.

(6) Peng, K.; Jie, J.; Zhang, W.; Lee, S.-T. *Appl. Phys. Lett.* **2008**, *93*, 033105.

(7) Chan, C. K.; Peng, H.; Liu, G.; McIlwrath, K.; Zhang, X. F.; Huggins, R. A.; Cui, Y. *Nat. Nanotechnol.* **2008**, *3*, 31−35.

(8) Javey, A.; Nam, S.-W.; Friedman, R. S.; Yan, H.; Lieber, C. M. *Nano Lett.* **2007**, *7*, 773.

(9) Kosloff, A.; Heifler, O.; Granot, E.; Patolsky, F. *Nano Lett.* **2016**, *16*, 6960.

(10) Sandu, G.; Brassart, L.; Gohy, J.-F.; Pardoen, T.; Melinte, S.; Vlad, A. *ACS Nano* **2014**, *8*, 9427−9436.

(11) Sandu, G.; Coulombier, M.; Kumar, V.; Kassa, H. G.; Avram, I.; Ye, R.; Stopin, A.; Bonifazi, D.; Gohy, J.-F.; Leclere, P.; Gonze, X.; Pardoen, T.; Vlad, A.; Melinte, S. *Sci. Rep.* **2018**, *8*, 9794.

(12) Lee, J.-H.; Zhang, A.; You, S. S.; Lieber, C. M. *Nano Lett.* **2016**, *16*, 1509.

(13) Zimmerman, J. F.; Murray, G. F.; Wang, Y.; Jumper, J. M.; Austin, J. R.; Tian, B. *Nano Lett.* **2015**, *15*, 5492.

(14) Kim, W.; Ng, J. K.; Kunitake, M. E.; Conklin, B. R.; Yang, P. *J. Am. Chem. Soc.* **2007**, *129*, 7228−7229.

(15) Shalek, A. K.; et al. *Nano Lett.* **2012**, *12*, 6498.

(16) Jeong, H.-E.; Kim, I.; Karam, P.; Choi, H.-J.; Yang, P. *Nano Lett.* **2013**, *13*, 2864.

(17) Xie, X.; Xu, A. M.; Angle, M. R.; Tayebi, N.; Verma, P.; Melosh, N. A. *Nano Lett.* **2013**, *13*, 6002.

(18) Huang, Z.; Geyer, N.; Werner, P.; de Boor, J.; Gösele, U. *Adv. Mater.* **2011**, *23*, 285−308.

(19) Hochbaum, A. I.; Chen, R.; Delgado, R. D.; Liang, W.; Garnett, E. C.; Najarian, M.; Majumdar, A.; Yang, P. *Nature* **2008**, *451*, 163−167.

(20) Tian, B.; Xie, P.; Kempa, T. J.; Bell, D. C.; Lieber, C. M. *Nat. Nanotechnol.* **2009**, *4*, 824−829.

(21) Huang, Z.; Zhang, X.; Reiche, M.; Liu, L.; Lee, W.; Shimizu, T.; Senz, S.; Gösele, U. *Nano Lett.* **2008**, *8*, 3046−3051.

(22) Holmes, J. D.; Johnston, K. P.; Doty, C.; Korgel, B. A. *Science* **2000**, *287*, 1471−1473.

(23) Duţu, C. A.; Vlad, A.; Reckinger, N.; Flandre, D.; Raskin, J.-P.; Melinte, S. *Appl. Phys. Lett.* **2014**, *104*, 023502.

(24) Yeom, J.; Ratchford, D.; Field, C. R.; Brintlinger, T. H.; Pehrsson, P. E. *Adv. Funct. Mater.* **2014**, *24*, 106−116.

(25) Huang, Z.; Shimizu, T.; Senz, S.; Zhang, Z.; Geyer, N.; Gösele, U. *J. Phys. Chem. C* **2010**, *114*, 10683−10690.

(26) Chiappini, C.; Liu, X.; Fakhoury, J. R.; Ferrari, M. *Adv. Funct. Mater.* **2010**, *20*, 2231−2239.

(27) Sivakov, V. A.; Brönstrup, G.; Pecz, B.; Berger, A.; Radnoczi, G. Z.; Krause, M.; Christiansen, S. H. *J. Phys. Chem. C* **2010**, *114*, 3798−3803.

(28) Peng, K.-Q.; Yan, Y.-J.; Gao, S.-P.; Zhu, J. *Adv. Mater.* **2002**, *14*, 1164−1167.

DOI: 10.1021/acs.nanolett.9b02568
Nano Lett. XXXX, XXX, XXX−XXX

(29) Justo, J. F.; Menezes, R. D.; Assali, L. V. C. *Phys. Rev. B* **2007**, *75*, 045303.
(30) Jiang, J.-W.; Yang, N.; Wang, B.-S.; Rabczuk, T. *Nano Lett.* **2013**, *13*, 1670−1674.
(31) Jiang, J.-W.; Rabczuk, T. *Appl. Phys. Lett.* **2013**, *102*, 123104.
(32) Vlad, A.; Frölich, A.; Zebrowski, T.; Duţu, C. A.; Busch, K.; Melinte, S.; Wegener, M.; Huynen, I. *Adv. Funct. Mater.* **2013**, *23*, 1164−1171.
(33) Schnaider, L.; Brahmachari, S.; Schmidt, N. W.; Mensa, B.; Shaham-Niv, S.; Bychenko, D.; Adler-Abramovich, L.; Shimon, L. J. W.; Kolusheva, S.; DeGrado, W. F.; Gazit, E. *Nat. Commun.* **2017**, *8*, 1365.
(34) Elgeti, J.; Winkler, R. G.; Gompper, G. *Rep. Prog. Phys.* **2015**, *78*, 056601.
(35) Bechinger, C.; Di Leonardo, R.; Löwen, H.; Reichhardt, C.; Volpe, G.; Volpe, G. *Rev. Mod. Phys.* **2016**, *88*, 045006.
(36) Nawroth, J. C.; Guo, H.; Koch, E.; Heath-Heckman, E. A. C.; Hermanson, J. C.; Ruby, E. G.; Dabiri, J. O.; Kanso, E.; McFall-Ngai, M. *Proc. Natl. Acad. Sci. U. S. A.* **2017**, *114*, 9510.
(37) Chen, Y.; Li, L.; Zhang, C.; Tuan, C.-C.; Chen, X.; Gao, J.; Wong, C.-P. *Nano Lett.* **2017**, *17*, 1014−1019.
(38) Kim, J.; Kim, Y. H.; Choi, S.-H.; Lee, W. *ACS Nano* **2011**, *5*, 5242−5248.
(39) Huang, Z.; Shimizu, T.; Senz, S.; Zhang, Z.; Zhang, X.; Lee, W.; Geyer, N.; Gösele, U. *Nano Lett.* **2009**, *9*, 2519−2525.
(40) Chen, H.; Wang, H.; Zhang, X.-H.; Lee, C.-S.; Lee, S.-T. *Nano Lett.* **2010**, *10*, 864−868.
(41) Chang, C.; Sakdinawat, A. *Nat. Commun.* **2014**, *5*, 4243.
(42) Day, R. W.; Mankin, M. N.; Gao, R.; No, Y.-S.; Kim, S.-K.; Bell, D. C.; Park, H.-G.; Lieber, C. M. *Nat. Nanotechnol.* **2015**, *10*, 345.
(43) Christesen, J. D.; Pinion, C. W.; Grumstrup, E. M.; Papanikolas, J. M.; Cahoon, J. F. *Nano Lett.* **2013**, *13*, 6281.
(44) Hildreth, O. J.; Lin, W.; Wong, C. P. *ACS Nano* **2009**, *3*, 4033.
(45) Zimmerman, J. F.; Parameswaran, R.; Murray, G.; Wang, Y.; Burke, M.; Tian, B. *Sci. Adv.* **2016**, *2*, No. e1601039.
(46) Liu, D.; Yi, C.; Wang, K.; Fong, C.-C.; Wang, Z.; Lo, P. K.; Sun, D.; Yang, M. *ACS Appl. Mater. Interfaces* **2013**, *5*, 13295−13304.
(47) Charles-Orszag, A.; et al. *Nat. Commun.* **2018**, *9*, 4450.
(48) Mager, M. D.; LaPointe, V.; Stevens, M. M. *Nat. Chem.* **2011**, *3*, 582.
(49) Guo, D.; Ji, X.; Wang, H.; Sun, B.; Chu, B.; Shi, Y.; Su, Y.; He, Y. *J. Mater. Chem. B* **2018**, *6*, 3876−3883.
(50) Geyer, N.; Fuhrmann, B.; Huang, Z.; de Boor, J.; Leipner, H. S.; Werner, P. *J. Phys. Chem. C* **2012**, *116*, 13446−13451.
(51) Kong, L.; Dasgupta, B.; Ren, Y.; Mohseni, P. K.; Hong, M.; Li, X.; Chim, W. K.; Chiam, S. Y. *Sci. Rep.* **2016**, *6*, 36582.
(52) Lai, R. A.; Hymel, T. M.; Narasimhan, V. K.; Cui, Y. *ACS Appl. Mater. Interfaces* **2016**, *8*, 8875−8879.
(53) Bazant, M. Z. *Acc. Chem. Res.* **2013**, *46*, 1144−1160.
(54) Mai, T. T.; Lai, C. Q.; Zheng, H.; Balasubramanian, K.; Leong, K. C.; Lee, P. S.; Lee, C.; Choi, W. K. *Langmuir* **2012**, *28*, 11465−11471.
(55) Shen, J.; Yang, X. *Discrete Cont. Dyn. A* **2010**, *28*, 1669−1691.
(56) Guyer, J. E.; Boettinger, W. J.; Warren, J. A.; McFadden, G. B. *Phys. Rev. E* **2004**, *69*, 021603.
(57) Chen, Y.; Zhang, C.; Li, L.; Tuan, C.-C.; Wu, F.; Chen, X.; Gao, J.; Ding, Y.; Wong, C.-P. *Nano Lett.* **2017**, *17*, 4304−4310.
(58) Kim, Y.; Tsao, A.; Lee, D. H.; Maboudian, R. *J. Mater. Chem. C* **2013**, *1*, 220−224.

DOI: 10.1021/acs.nanolett.9b02568
Nano Lett. XXXX, XXX, XXX−XXX